

Supporting Information for Blue microlasers integrated on a photonic platform on silicon

Farsane Tabataba-Vakili,^{†,‡} Laetitia Doyennette,[¶] Christelle Brimont,[¶] Thierry Guillet,[¶] Stéphanie Rennesson,[§] Eric Frayssinet,[§] Benjamin Damilano,[§] Jean-Yves Duboz,[§] Fabrice Semond,[§] Iannis Roland,^{†,||} Moustafa El Kurdi,[†] Xavier Checoury,[†] Sébastien Sauvage,[†] Bruno Gayral,[‡] and Philippe Boucaud^{*,†,§}

[†]*Centre de Nanosciences et de Nanotechnologies, CNRS, Univ. Paris-Sud, Université Paris-Saclay, F-91405 Orsay, France.*

[‡]*CEA, INAC-PHELIQS, Nanophysique et semiconducteurs group, Univ. Grenoble Alpes, F-38000 Grenoble, France.*

[¶]*Laboratoire Charles Coulomb (L2C), Université de Montpellier, CNRS, F-34095 Montpellier, France.*

[§]*Université Côte d'Azur, CRHEA-CNRS, F-06560 Valbonne, France.*

^{||}*Current address: Université Paris Diderot-Paris7, F-75013 Paris, France.*

E-mail: philippe.boucaud@crhea.cnrs.fr

The supporting information includes 10 pages and 10 figures.

FDTD simulations

We have performed 3D finite-difference time-domain (FDTD) simulations for our fabricated microdisk photonic circuits using a resolution of 16 pixels per wavelength in the material. The simulated disk has a $3 \mu\text{m}$ diameter, an intrinsic Q factor of $Q_{int} = 3600$, and a bus waveguide with a 90° bending angle. The Q factor is limited by artificial absorption introduced in the disk to make the values more realistic. The structure consists of a two layer stack of 100 nm AlN ($n = 2.12$) and 410 or 310 nm of GaN ($n = 2.46$) for the disk and waveguide, respectively. A 2D in-plane visualization of a simulated device with a gap of $g = 50$ nm and a waveguide width of $w = 133$ nm is shown in figure S1, depicting the H_z field of a first order radial mode with azimuthal order $m = 48$.

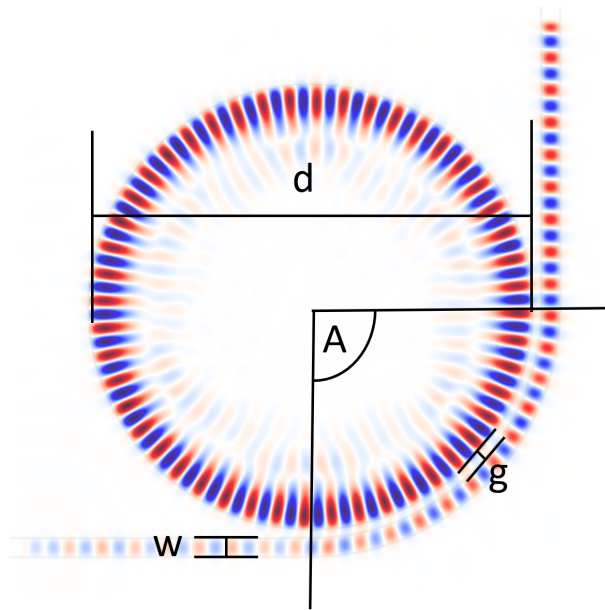


Figure S1: Simulation of the H_z field of a $d = 3 \mu\text{m}$ diameter disk for a first order radial mode with azimuthal order $m = 48$. The waveguide is bent at a $A = 90^\circ$ angle, the gap is $g = 50$ nm and the waveguide width is $w = 133$ nm.

In the simulation the disk is passive and we inject a Gaussian beam on the left side of the waveguide. We determine the transmission by taking the ratio between the flux at the end of the coupling waveguide and dividing it by the flux at the end of a straight uncoupled waveguide of the same width. The transmission formula is given by

$$T = \left(\frac{1 - \frac{Q_{int}}{Q_c}}{1 + \frac{Q_{int}}{Q_c}} \right)^2, \quad (1)$$

where Q_{int} is the intrinsic quality factor and Q_c is the coupling quality factor. A transmission spectrum is depicted in figure S2 a) and compared to an experimental emission spectrum in figure S2 b). The mode spacing between first order radial modes is 5 – 6 nm and the mode positions match well between simulation and experiment. The azimuthal number of each mode is clearly identified by performing simulations for a 1 nm wavelength range around each mode and counting the nodes in the H_z field.

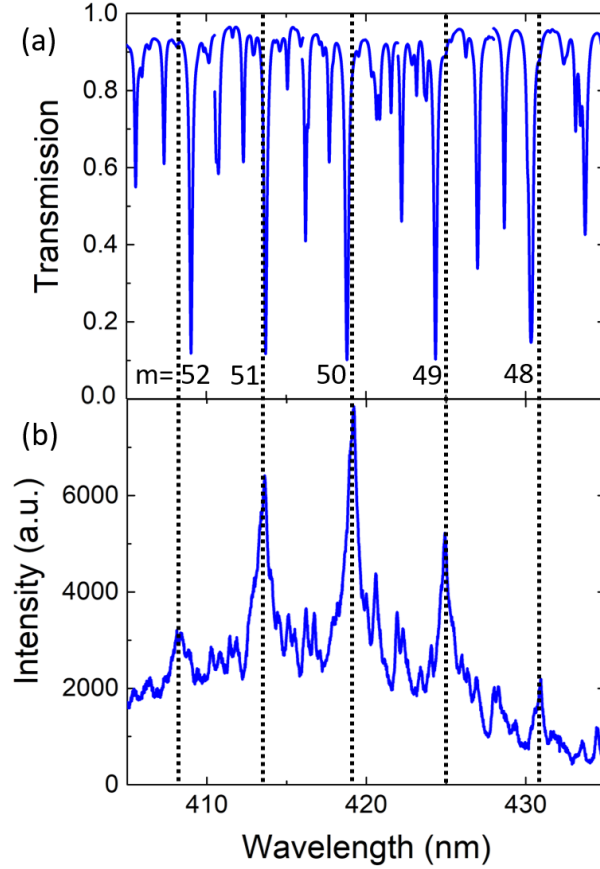


Figure S2: Comparison of a) simulation and b) measurement for a 3 μm diameter disk. The mode positions match well and the azimuthal numbers of the first order radial modes is clearly identified.

In figure S3 a) the transmission spectra for one first order radial mode are depicted for different gap sizes. For a gap of 80, 100, and 120 nm the system is undercoupled, at 50 nm it

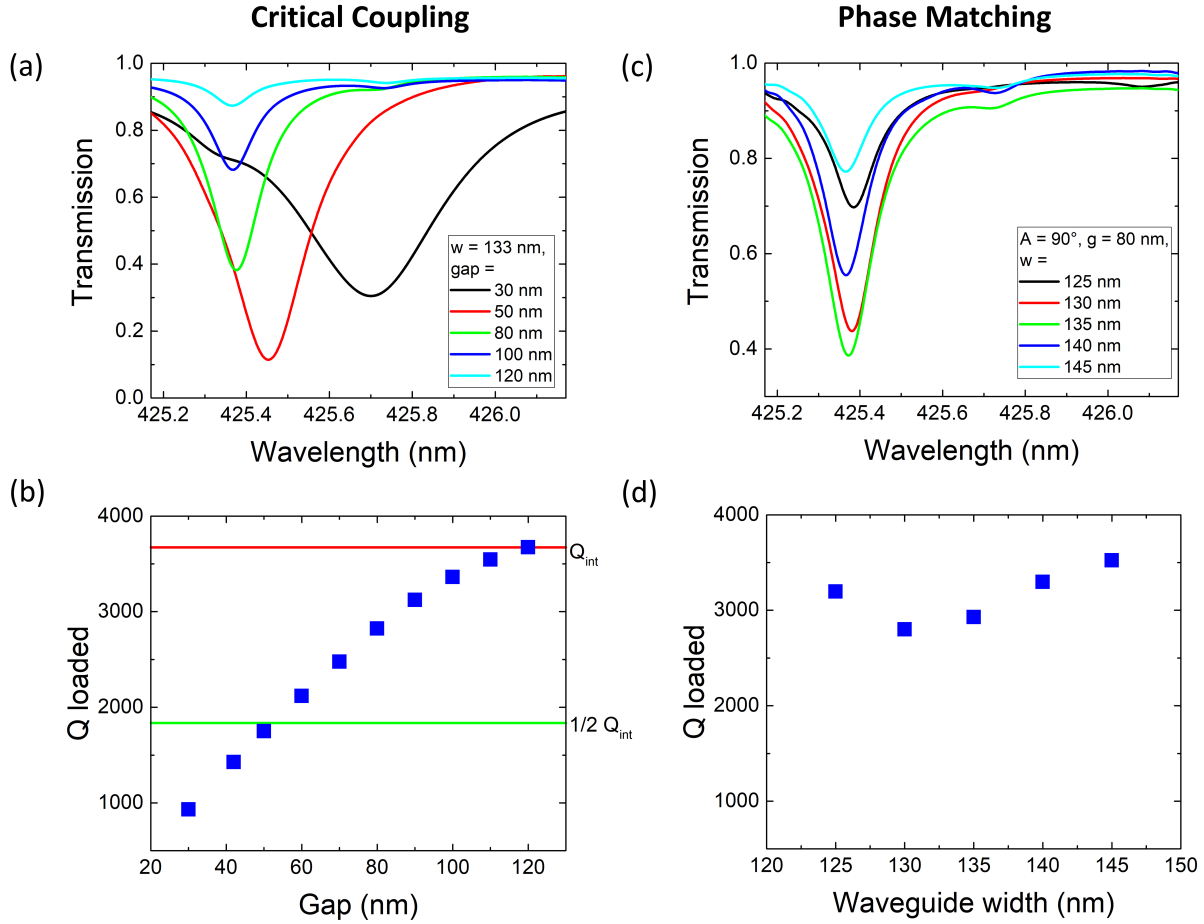


Figure S3: FDTD simulations of critical coupling and phase matching showing transmission and loaded Q factor of devices with a 3 μm diameter disk with $A = 90^\circ$ for different gap sizes and waveguide widths a) Transmission for devices with $w = 133$ nm and five different gaps showing the undercoupled (80, 100, and 120 nm), critically coupled (50 nm) and over coupled (30 nm) regime. b) Loaded Q factor in dependence of gap size showing the degradation of the Q factor with increased coupling. $Q_{loaded} \approx Q_{int}$ for $g = 120$ nm and $Q_{loaded} \approx 1/2 Q_{int}$ at $g = 50$ nm. c) Transmission for devices with a gap of 80 nm and different waveguide widths showing phase matching around $w = 135$ nm. d) Loaded Q factor for different waveguide widths demonstrating its independence from phase matching far away from critical coupling.

is very close to critical coupling and a transmission minimum, and at 30 nm it is overcoupled. Figure S3 b) shows the loaded Q factor over the gap size for gaps from 30 to 120 nm. For large gaps $Q_{loaded} \approx Q_{int}$. The loaded Q factor decreases with decreasing gap size and reaches $Q_{loaded} \approx 1/2 Q_{int}$ at critical coupling around $g = 50$ nm. A further requirement for critical coupling is phase matching, which can be achieved for different combinations of g and w and is given at $g = 50$ nm and $w = 133$ nm. Figure S3 c) shows simulated transmission spectra for devices with a gap of 80 nm and different waveguide widths. For a width of around 135 nm a transmission minimum can be observed, which corresponds to phase matching. The corresponding loaded Q factor (depicted in figure S3 d)) is not significantly degraded by phase matching when the system is far away from critical coupling, as is the case for a gap of 80 nm. Meanwhile we can observe the very high sensitivity of this system in the blue spectral range, as a small deviation of few tens of nm very rapidly degrade the transmission, i.e. the coupling ratio and visibility of the modes.

The simulation were performed for devices with a bending angle of 90° but the results are similar at smaller angles and for straight waveguides. With decreasing waveguide bending angle the phase matching condition becomes less critical due to the reduced coupling length. Experimentally we are far away from critical coupling with gap sizes between 80 and 120 nm. Consequently, there is only a small degradation of the loaded Q factor, which is close to the intrinsic one. In this undercoupled regime the effect of phase matching on the Q factor is also minor, which allows us to observe lasing.

Figure S4 a) shows FDTD simulations of devices with different waveguide heights between 250 nm and 510 nm over a 30 nm wavelength range, depicting various modes. A zoom-in onto the mode at 425.5 nm is shown in figure S4 b). With a slight decrease in waveguide thickness as compared to the disk thickness, the coupling strength increases and a larger transmission dip is observed, while the mode position shifts for very thin waveguides. The transmission over the waveguide height for the mode at 425.5 nm is shown in figure S4 c). The transmission minimum is observed at a waveguide height of 410 nm, which is close to

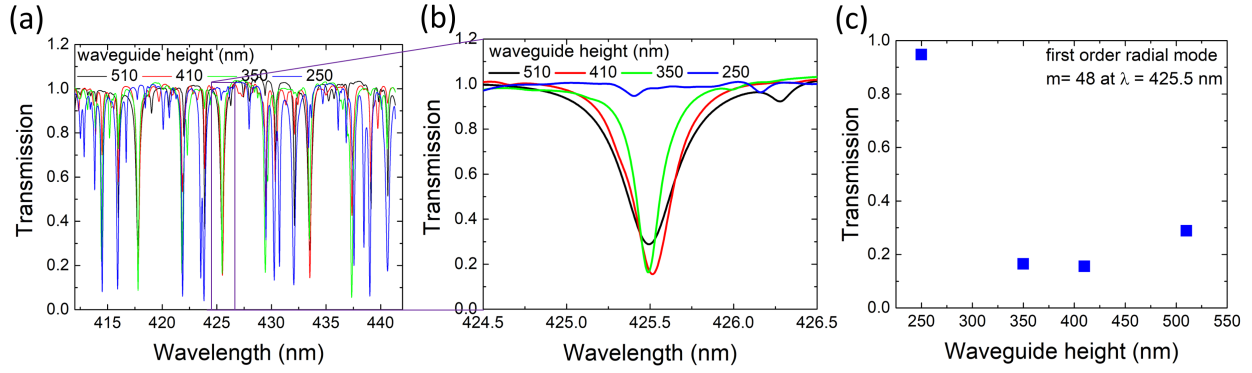


Figure S4: FDTD simulation of the influence of the waveguide height on the coupling strength. a) Transmission over a 30 nm wavelength range for a waveguide height between 250 nm and 510 nm. b) Zoom-in on the first-order radial mode with azimuthal order $m = 48$ at 425.5 nm. c) Transmission over waveguide height for the same mode as in b).

our nominal etch depth.

An FDTD simulation of an outcoupling grating is shown in figure S5 with a period of 195 nm and a fill-factor of 60%. The outcoupling efficiency is 6% at 417 nm.

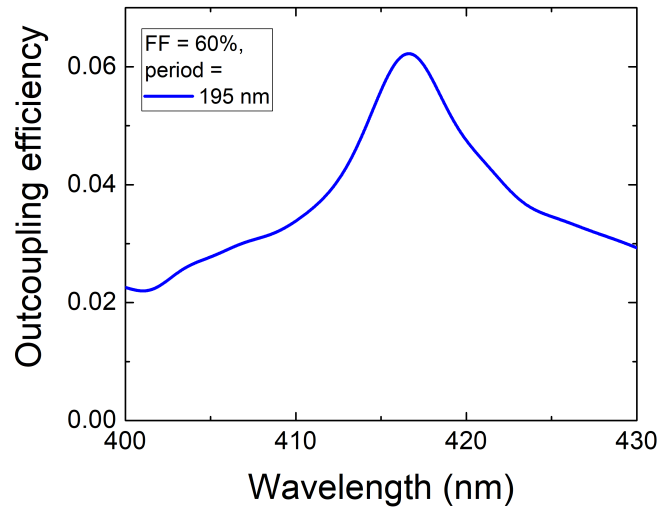


Figure S5: FDTD simulation of an out-coupling grating with a 195 nm period and a fill-factor of 60%, giving an outcoupling efficiency of 6% at 417 nm.

Additional micro-PL results

Spectra of devices with $3\ \mu\text{m}$ diameter disks, 90° bent waveguides and a gap of $90\ \text{nm}$ are shown in figure S6 b) for waveguide widths of $115\ \text{nm}$ and $125\ \text{nm}$. Zoom-ins of both curves are shown in figure S6 a) and c), respectively, depicting Lorentzian fits of several modes, giving loaded Q factors between 1200 and 1900 , which are very comparable to devices with $5\ \mu\text{m}$ diameter, shown in figure 3 in the manuscript.

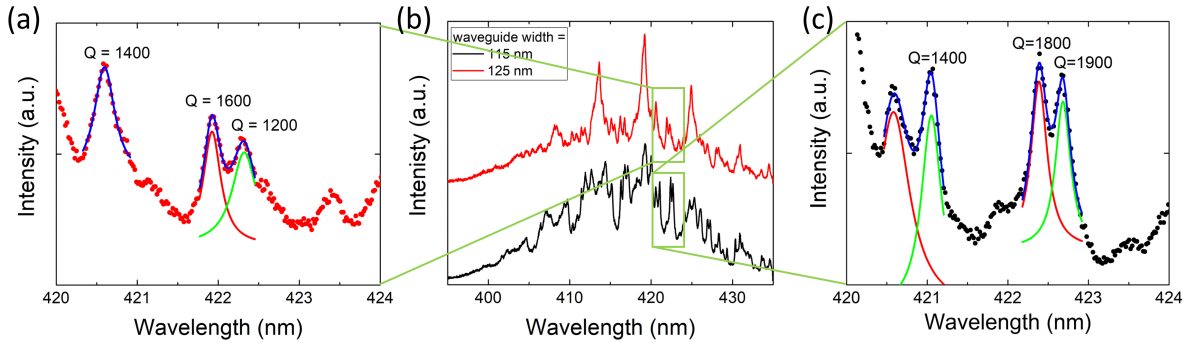


Figure S6: Loaded Q factor of two devices with a disk diameter of $3\ \mu\text{m}$, a waveguide bending angle of 90° , a gap of $90\ \text{nm}$, and waveguide widths of 115 to $125\ \text{nm}$. a) Zoom-in of the $w = 125\ \text{nm}$ curve and Lorentzian fits giving loaded Q factors of 1200 to 1600 . b) Full spectra of both devices. c) Zoom-in of the $w = 115\ \text{nm}$ curve and Lorentzian fits giving loaded Q factors of 1400 to 1900 .

Using the same setup as described in the manuscript, we performed pulsed measurements for a $4\ \mu\text{m}$ diameter disk without a waveguide with a lasing wavelength of $416.5\ \text{nm}$ and a threshold of $2.6\ \text{mJ}/\text{cm}^2$ per pulse. Figure S7 a) shows an S-shaped increase of the mode amplitude with pump energy and linewidth narrowing is observed in b).

Figure S8 shows the CCD intensity map and corresponding SEM image of a device, also depicted in figure 2 a) in the manuscript with higher over-saturation of the CCD map to highlight the emission at the gratings, which is marked in red.

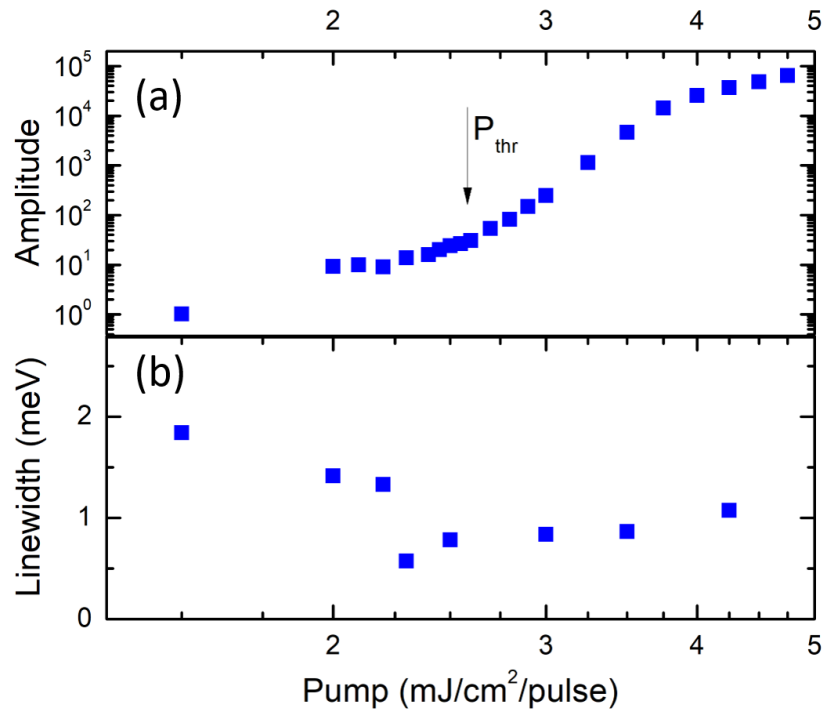


Figure S7: Pump energy-dependent measurement of a 4 μm diameter microdisk laser without a waveguide fabricated on the same wafer, showing a) amplitude and b) linewidth of the lasing mode at 416.5 nm.

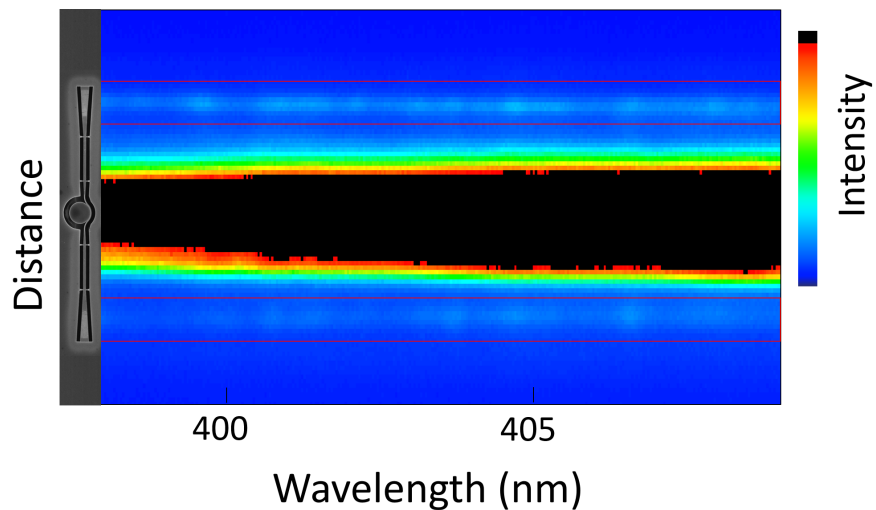


Figure S8: Over-saturated intensity map of the CCD with corresponding SEM image of a device on the left side. Same image as figure 2 a) in the manuscript, but with a different color scale to highlight the emission at the gratings. The gratings are indicated in red.

Additional microscope and SEM images

The pedestal shape varies based on the device geometry, due to the first ICP etch leaving a thin layer of AlN remaining. For devices with a $3\ \mu\text{m}$ diameter disk (shown in figure S9 a)), there is no pedestal remaining after the underetch and the disk is being held in place by the thin AlN layer. This explains the higher threshold and worse thermal management observed as compared to conventional mushroom-type microdisks. For a $5\ \mu\text{m}$ diameter disk and a 90° waveguide angle (as shown in figure S9 b)) we observe a triangular decentralized pedestal that could explain that lasing is not observed for such devices, due to mode leakage into the pedestal.

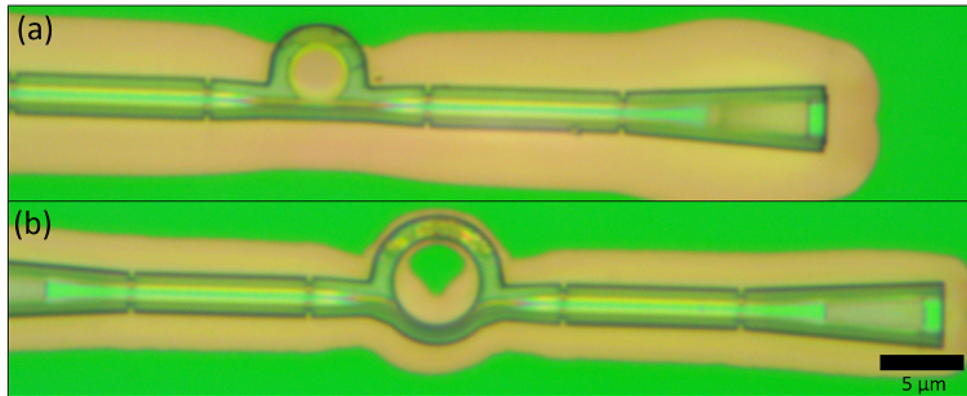


Figure S9: Optical microscope images of a) a $3\ \mu\text{m}$ diameter disk with a straight waveguide and b) a $5\ \mu\text{m}$ diameter disk with a 90° bent waveguide. The underetch and silicon pedestal are visible.

Close-up SEM images of various components of the photonic circuit are shown in figure S10 a)-d). All components are showing some roughness from the processing.

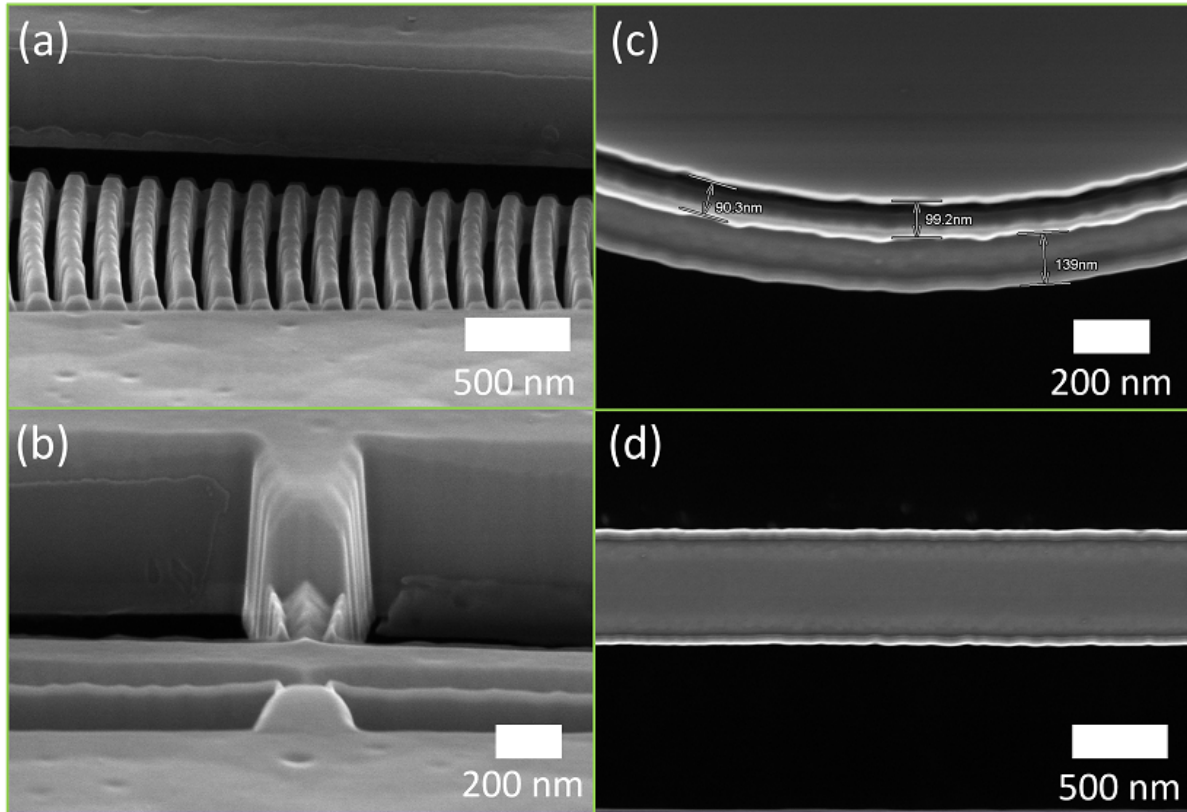


Figure S10: Close-up SEM images of various parts of the photonic circuit. a) Side-view of a grating coupler at a 20° angle. b) Side-view of a tether and waveguide at a 20° angle. c) Top-view of a disk and waveguide depicting a gap of 90 - 100 nm. d) Top-view of the wide part of a waveguide.